Science Advances
AAAS

advances.sciencemag.org/cgi/content/full/5/2/eaav4316/DC1

Supplementary Materials for

High-speed imaging of ice nucleation in water proves the existence of active sites

Mark A. Holden*, Thomas F. Whale, Mark D. Tarn, Daniel O'Sullivan, Richard D. Walshaw, Benjamin J. Murray, Fiona C. Meldrum*, Hugo K. Christenson*

*Corresponding author. Email: m.a.holden@leeds.ac.uk (M.A.H.); f.meldrum@leeds.ac.uk (F.C.M.); h.k.christenson@leeds.ac.uk (H.K.C.)

Published 1 February 2019, *Sci. Adv.* **5**, eaav4316 (2019)
DOI: 10.1126/sciadv.aav4316

The PDF file includes:

Other Supplementary Material for this manuscript includes the following:

(available at advances.sciencemag.org/cgi/content/full/5/2/eaav4316/DC1)

Movie S1 (.avi format). Ice nucleation from the melt on the (010) face of microcline feldspar.
Movie S2 (.avi format). Ice nucleation from the melt on the (001) face of microcline feldspar.
Movie S3 (.avi format). Ice nucleation from the melt on α-quartz.
Movie S4 (.mp4 format). Movie demonstrating how freeze-thaw video microscopy can be used for direct observation of site-specific ice nucleation in supercooled water.

Supplementary Text

Section S1. Time dependence of nucleation

The graphs displayed in fig. S5C show the temperatures that ice nucleated at the most active site in a drop during 6 freeze-thaw experiments. With the ability to identify where nucleation starts, it is possible to determine site specific freezing temperatures. In Fig. 5 and fig. S5A-B, these site specific temperatures are used to construct fraction frozen plots, and calculate temperature dependent nucleation rates for specific sites. In the case of the drops that freeze at lower temperatures, the data will be skewed to higher temperatures due to competition from other active sites within the drop. At higher temperatures, when only one site dominates freezing, the rate calculated will be more representative. In these experiments, it is assumed that no significant damage is done that alters the active region, since crystallisation in a porous medium is known to lead to frost damage. This assumption is rationalised by monitoring the freezing temperature over the course of the experiments, which did not change significantly. These experiments show that site specific nucleation rates can be obtained with careful experimental design, and this opens the possibility to calculate accurate nucleation rates that are specific to a single site.

The nucleation rates obtained from immersed particle experiments differ to those for single sites. The gradient of the freezing rate for bulk experiments is not equal to the gradients of the freezing rate for single site freezing. Instead, it is shallower, as shown in Fig. 5C. This difference demonstrates that this system is multiple component, i.e. that more than one type of active site exists. In this example, knowing that a single site is being observed in the experiments means that the gradient calculated from the freezing rate is that of a single component system, equivalent to λ as defined by Herbert et al. (*15*). On the other hand, the rate calculated from the bulk immersed particles gives ω, as defined by Vali (*16*). For a single component system, $\lambda = \omega$

(*15*). For a different alkali feldspar, BCS376, ω = 0.85 - 0.9 °C^{-1}, whilst λ = 3.4 °C^{-1}. Here, ω = 0.5 °C^{-1}, whilst λ = 1.7 - 3.4 °C^{-1}. This means that the normalised freezing rates calculated from bulk experiments are not equivalent to the nucleation rate, *J*. However, in the case of drops dominated by single sites, the rate of freezing calculated does give the nucleation rate. This demonstrates how this technique allows nucleation rates to be calculated for specific sites within complex multiple component systems.

Section S2. Nucleation at the contact line

Nucleation at the contact line, i.e. the air-water-surface interface, has been studied for samples where specific active sites were avoided, and many different freezing locations were recorded (*40*). In these experiments, no preference for the contact line was observed. However, when surfaces with texture were added, nucleation from the contact line was observed (*41*). Here, nucleation was not observed preferentially at the contact line. Instead, the active sites always dictated where freezing would occur. When these were at the edge of a droplet, freezing started from the contact line, whilst freezing would occur in the middle of the drop when this was where sites were located (fig. S9).

In these experiments, it is difficult to assign whether freezing at the edge of a drop is caused by true nucleation at the contact line, or communication from condensing liquid elsewhere on the surface; since the feldspar contains porous microtexture, it is possible that condensation of water could lead to this communication, which could influence measurements. In experiments where obvious condensation occurred, freezing events at the contact line were excluded, whereas if there was no observed condensation these events were included. In the experiments, the

temperature that the drop froze when the first ice growth was observed at the contact line was similar to the freezing temperature at other sites within the drop. When visible condensation was present, freezing from the contact line was typically at higher temperatures, suggesting communication from water that froze at a more active site outside the drop.

Section S3. Morphology of growing ice

The morphology of ice growth on the alkali feldspar depended on the crystal face observed. Ice growing on the (010) face of feldspar typically had greater contrast to that growing on the (001) face. Furthermore, the ice on the (010) was oriented in a broadly rectangular morphology, with a cross emanating from the nucleation site to each of the four corners of the rectangle (Fig. 1). Conversely, freezing on the (001) tended to proceed with curved trajectories. The growth of ice on quartz further differed to that on feldspar (Fig. 6). The rate of growth was consistent with measurements by Schremb et al. (*12*). In all of these experiments, the ice froze and grew with a dendritic morphology. This was in contrast to previous observations on silicon by Gurganus et al., where ice that froze within a droplet had a hexagonal morphology (*40*).

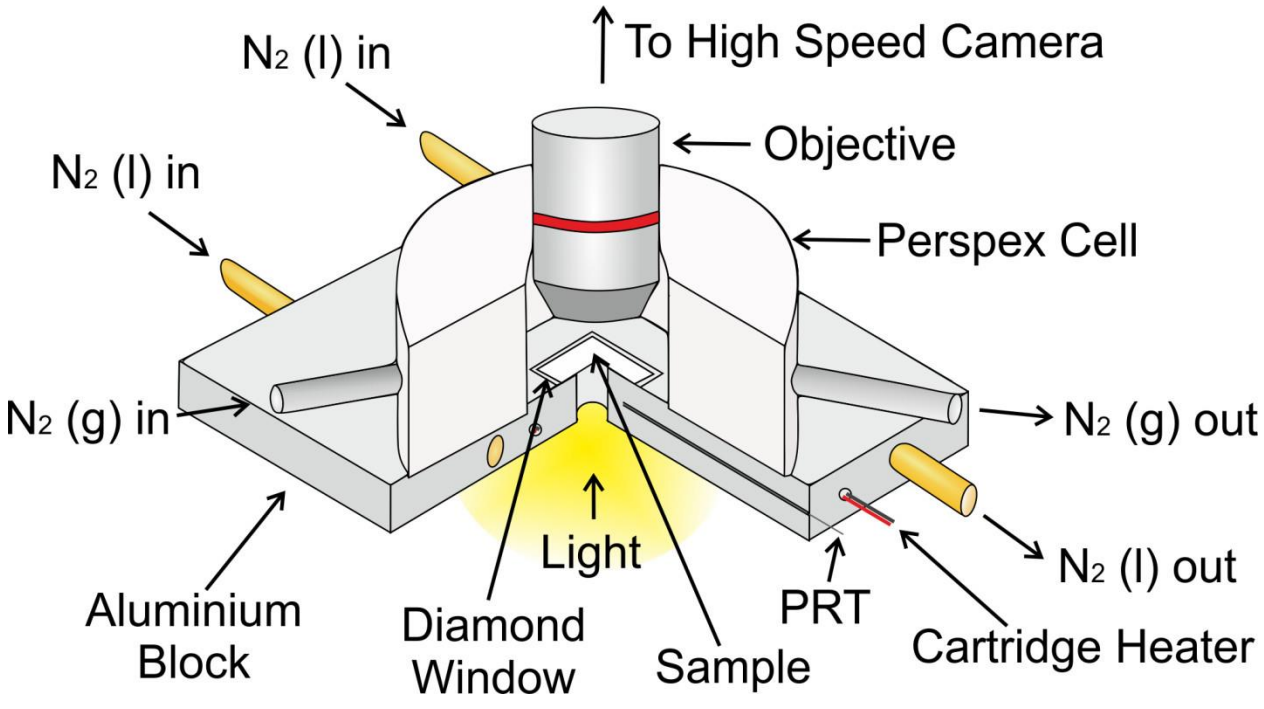

Fig. S1. Schematic of experimental setup. Schematic showing the stage used in freeze-thaw cryomicroscopy experiments performed on single drops of Milli-Q pipetted onto a feldspar surface.

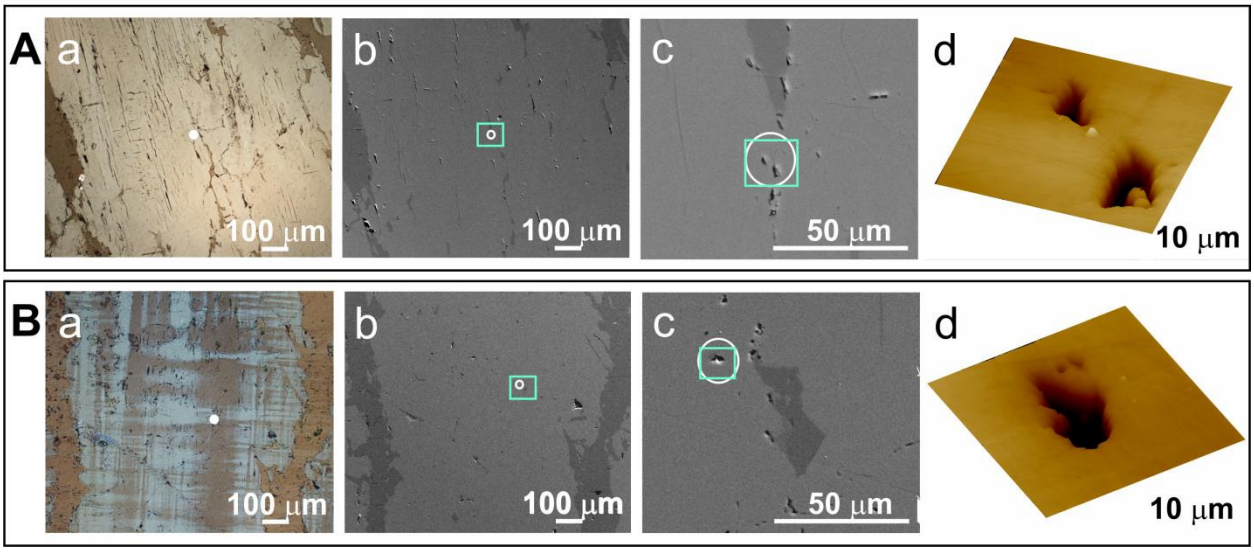

Fig. S2. Identification of feldspar active sites. (**A** and **B**) Light micrographs, electron micrographs and AFM micrographs showing two active sites identified high speed video microscopy experiments. Active sites are on (**A**) the (010) face, and (**B**) the (001) face. In each case, a topographic feature, either a crack or micropore, was present at the location where freezing began. In the lower magnification SEM images, the region that is shown in the higher magnification images is marked with a rectangle. The region investigated with AFM is highlighted in the higher magnification SEM micrograph by the rectangle. The circle shows the area in which ice nucleated.

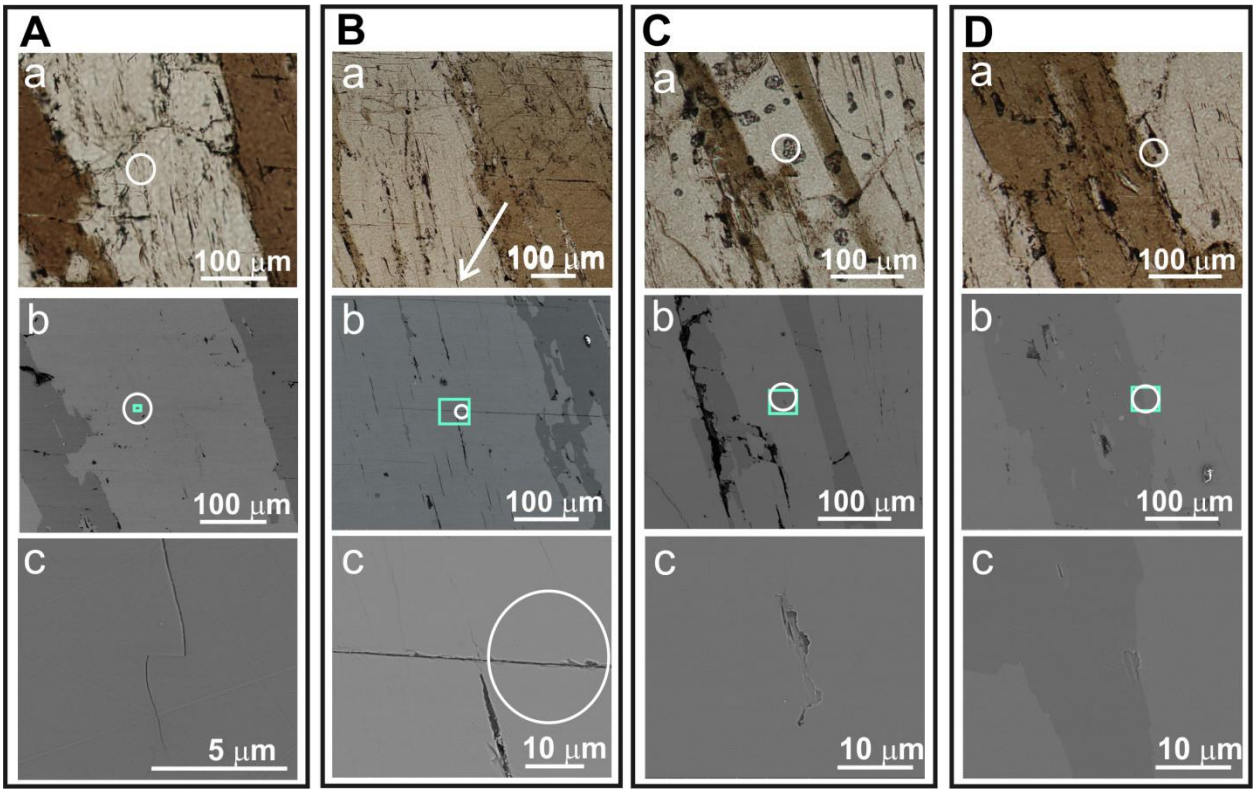

Fig. S3. Microscopy of feldspar active sites. (**A** to **D**) Light micrographs and electron micrographs showing several active sites identified during drop freezing experiments. In each case, a topographic feature, either a crack or micropore, was present at the location where freezing began. In the lower magnification SEM images in (b), the region that is shown in the higher magnification images in (c) is marked with a rectangle. The circle shows the area in which ice nucleated.

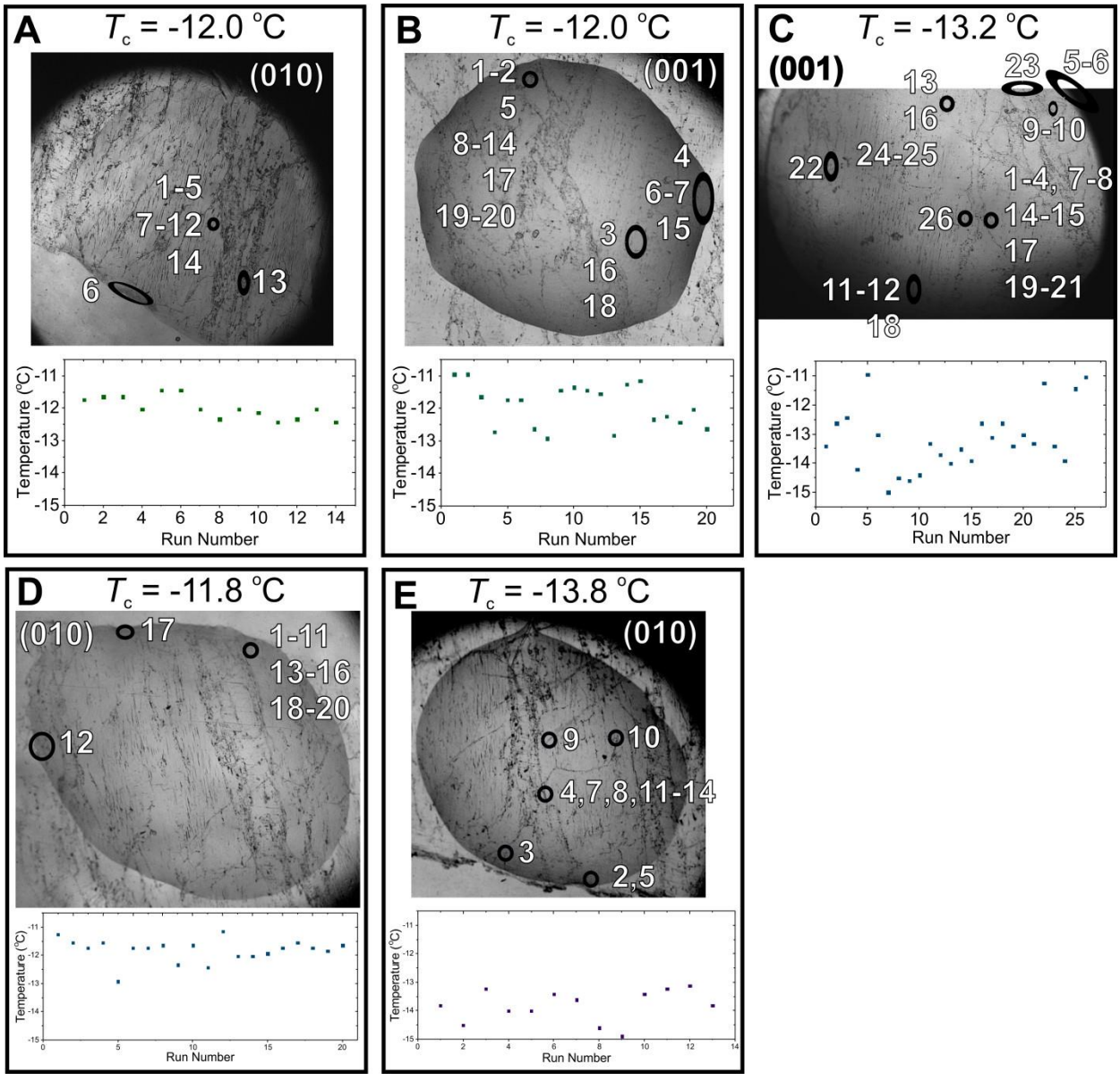

Fig. S4. Identification of active sites through freeze-thaw experiments. (**A** to **E**) Light micrographs showing the regions in which ice froze in several different freeze-thaw experiments on different regions of the feldspar surface. Each figure shows the regions, and the corresponding runs at which ice froze in that region. The freezing temperatures over the entire freeze-thaw experiment are shown below the light micrographs.

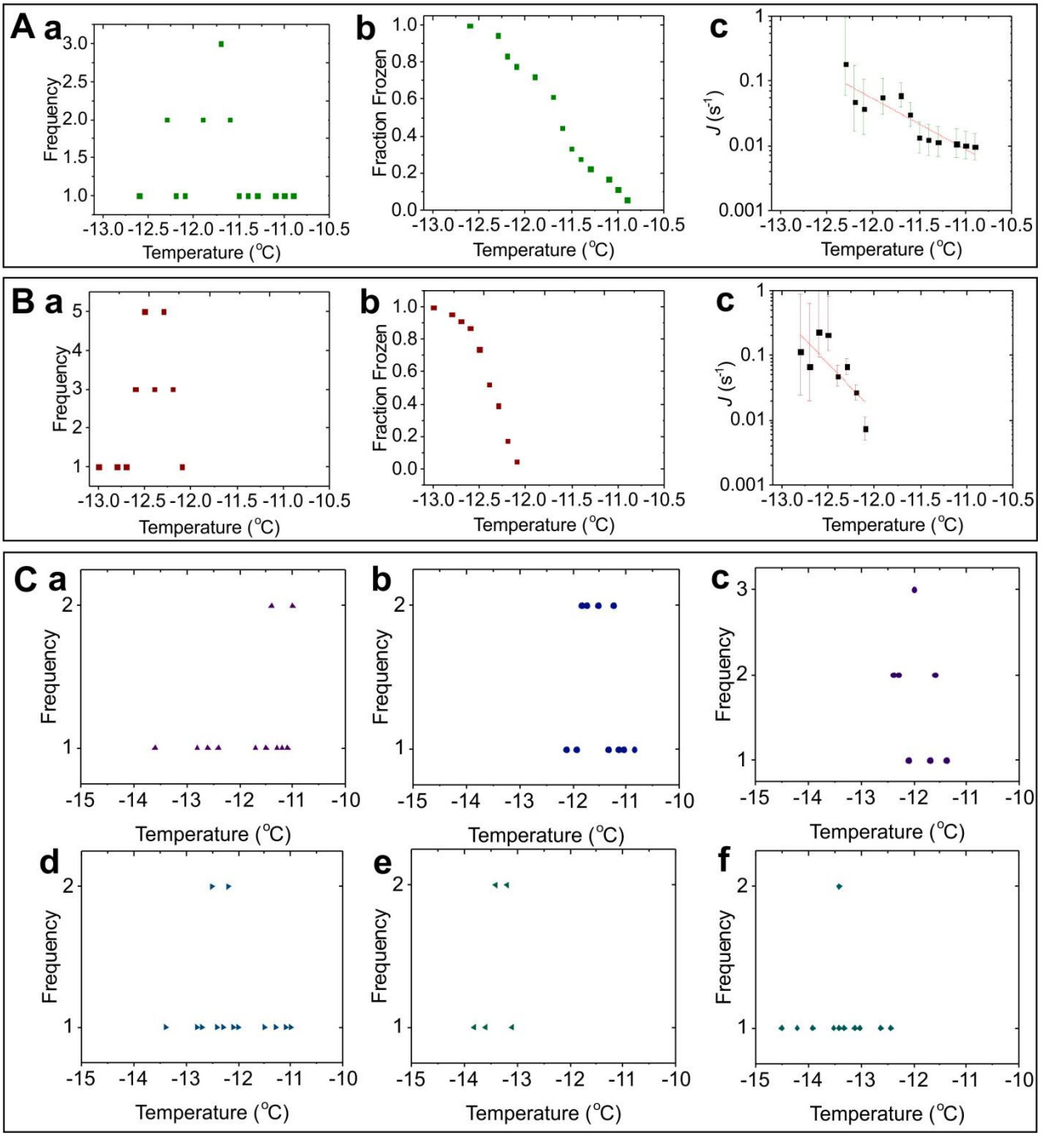

Fig. S5. Time dependence of nucleation. (**A** and **B**) (a) Probability density function (pdf) plots for freezing at two active sites, measured in two different freeze-thaw experiments. The site in (**A**) is the most active site in Fig. 3B (18/20 nucleation events, (010) face), and the site in (**B**) is the most active site in Fig. 3D (23/26 nucleation events, (001) face). The temperature measurements were made in 0.1 °C size bins, based on the experimental output. (b) Plot of

fraction frozen constructed from the pdf in (a). This plot treats each cycle in the freeze-thaw experiment as an individual drop in a freezing array, with each drop containing an identical active site. This plot assumes that the active site does not alter significantly over the course of the experiment. (c) Site specific nucleation rate plots for the active sites in (a). These give the actual nucleation rate, *J*, as opposed to bulk experiments, which only give a freezing rate due to the number of different sites present in an array. (**C**) (a-f) Probability density function (pdf) plots for other active sites measured during this series of experiments, demonstrating the possibility to measure site specific nucleation rates.

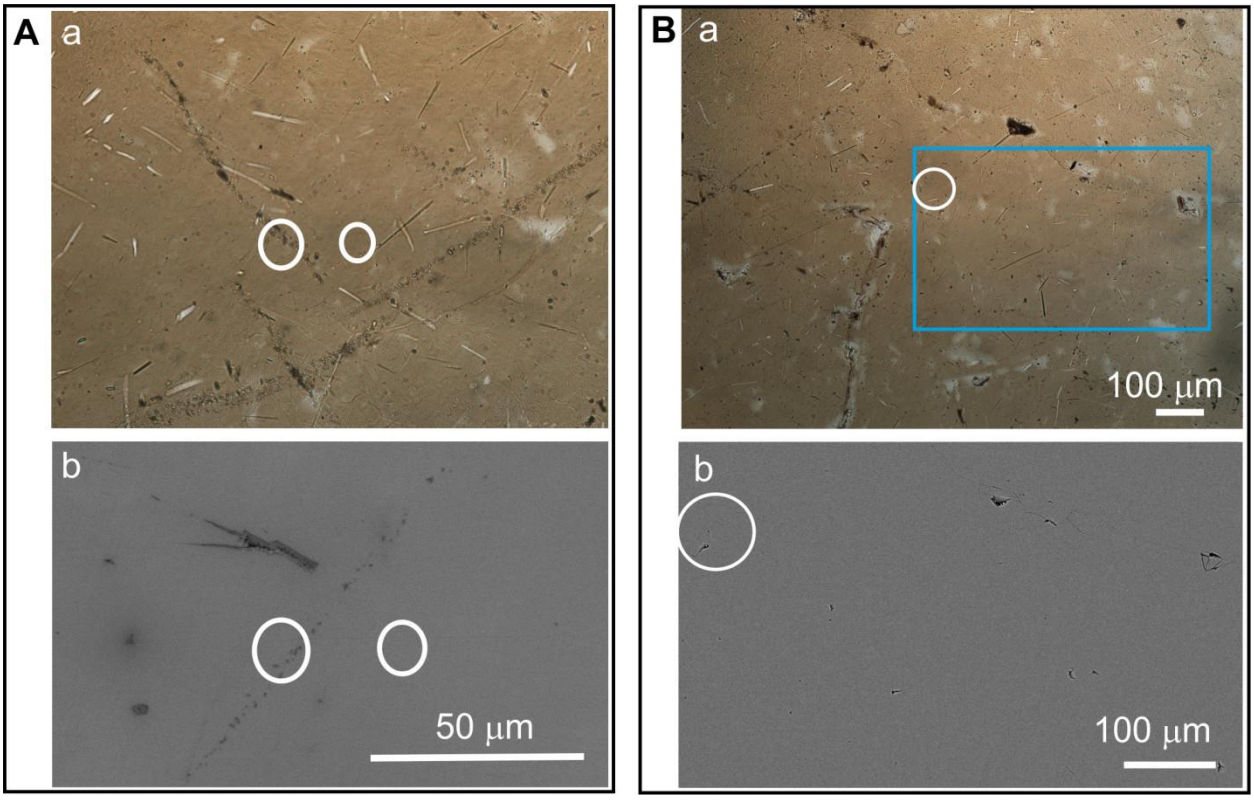

Fig. S6. Identification of rose quartz active sites. (**A** and **B**) Light micrographs and electron micrographs showing three active sites - two in **A**, one in **B** (highlighted by white ovals) - identified on rose quartz during cryomicroscopy experiments. In two cases, obvious topographic features are at the active site. Topography of various length scales was observed on the rose quartz thin sections, though the density of features was significantly lower than on feldspar.

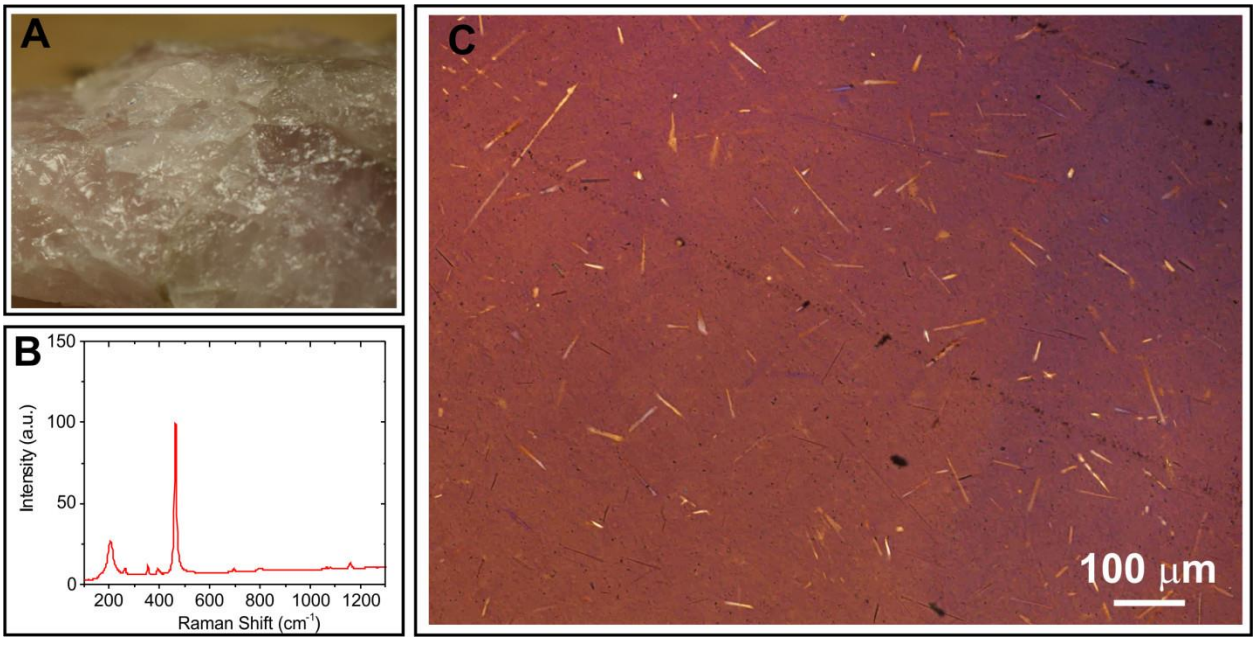

Fig. S7. Characterization of rose quartz. (**A**) Photograph of the rose quartz sample used in this study, demonstrating the lack of clear faceting on the crystal. (**B**) Raman spectrum obtained from a powdered rose quartz sample, used to confirm the mineral as α-quartz. (**C**) Light micrographs showing the surface of a thin section of rose quartz. Only Si and O, associated with the predominant SiO_2 of the quartz, were detected by EDX analysis.

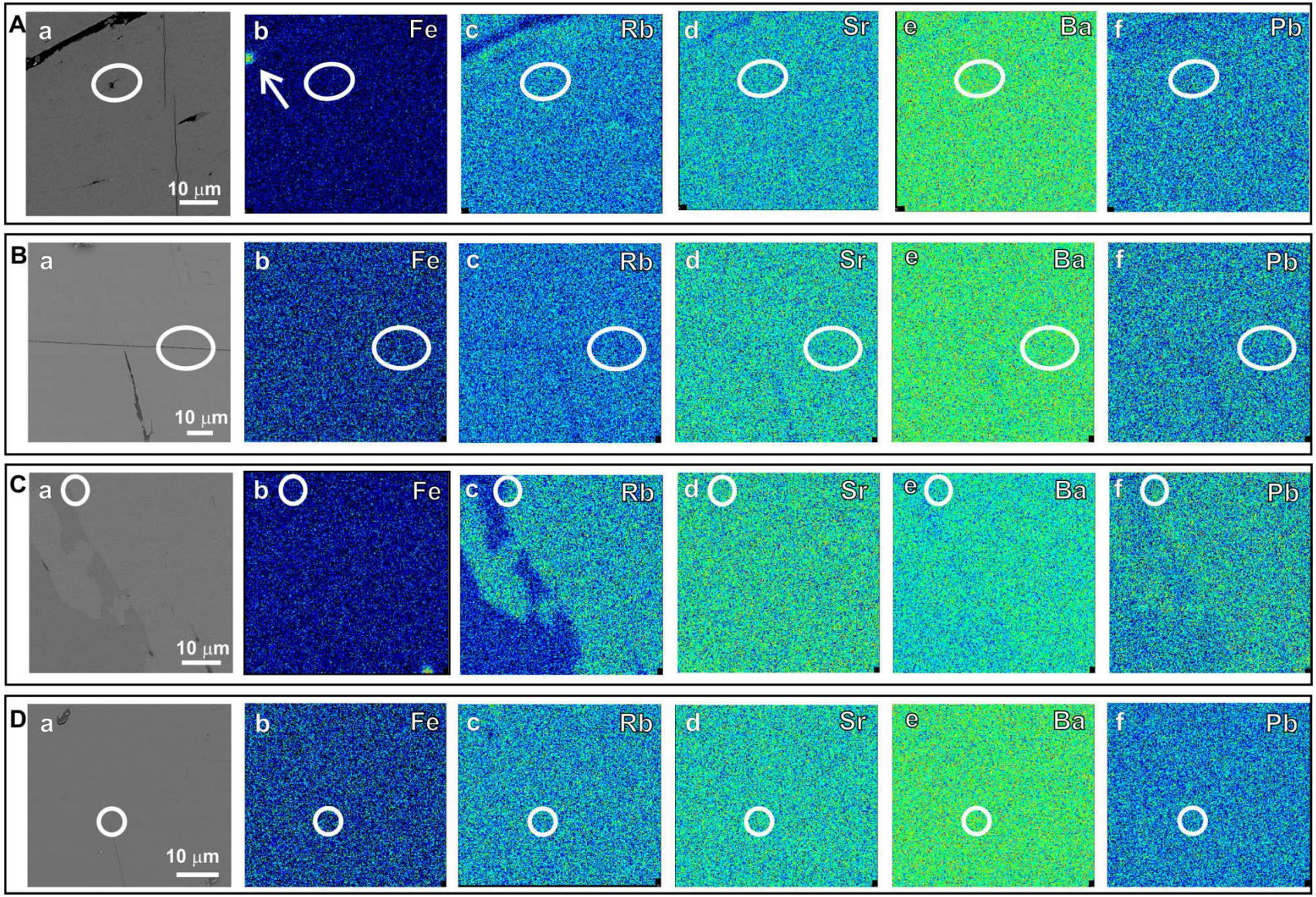
A
a
10 μm
b
Fe
c
Rb
d
Sr
e
Ba
f
Pb
B
a
10 μm
b
Fe
c
Rb
d
Sr
e
Ba
f
Pb
C
a
10 μm
b
Fe
c
Rb
d
Sr
e
Ba
f
Pb
D
a
10 μm
b
Fe
c
Rb
d
Sr
e
Ba
f
Pb

Fig. S8. WDS maps of active sites. (**A** to **D**) Micrographs of four different active site, identified using high speed cryomicroscopy, showing: (a) SEM micrographs of the area, with the active sites circled in white, (b-f) WDS maps taken for several elements commonly present at trace levels in alkali feldspars. The relative concentration of the element is plotted, with ‘cold’ colours (blue/green) showing low relative concentrations, and ‘hot’ colours (yellow/red) showing relatively high concentrations. In **A**(b), a ‘hot spot’ is seen in the Fe map, away from the active region, demonstrating the detection of an enhanced concentration of one of these species. These maps show that there are no increased concentrations of these elements at the active sites within the resolution of the technique, since there are no ‘hot spots’ in the active region.

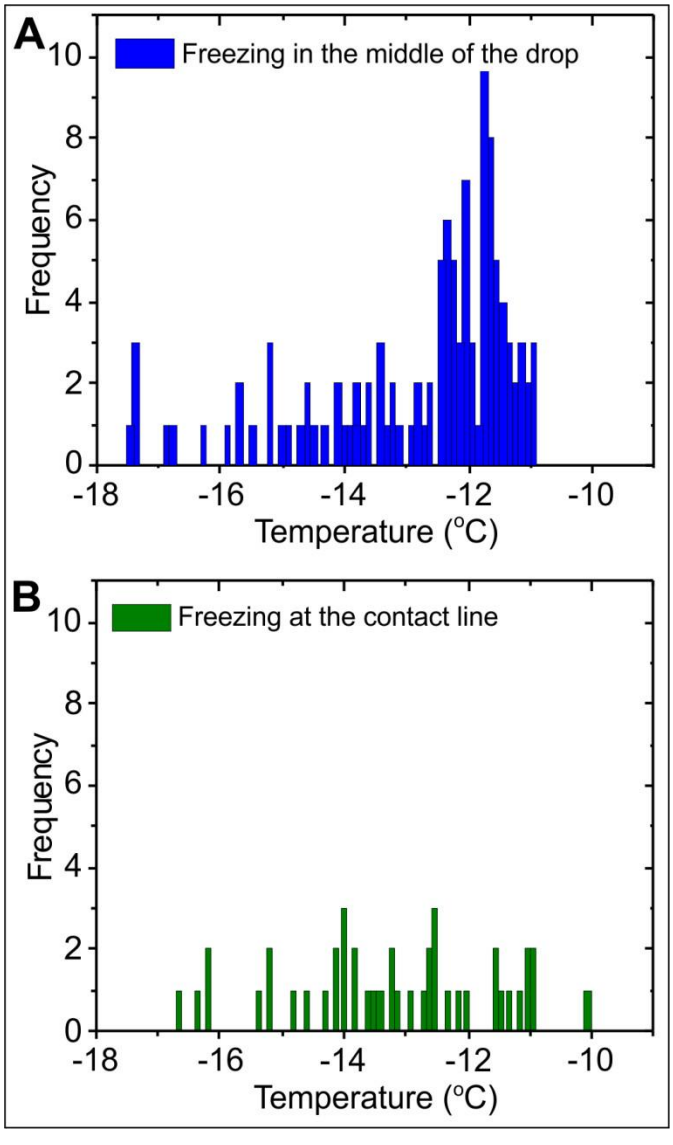

Fig. S9. Investigation of freezing at the three-phase line. (**A** and **B**) Plots showing the number of freezing events across all LD3 microcline feldspar experiments that began at the edge of the drop, on the three-phase line (water- air- surface interface), or contact line, compared to those that froze in the middle of the drop (water- surface interface).